ACS NANO
Cite This: ACS Nano 2018, 12, 7866−7874
www.acsnano.org

ARTICLE

Bimetallic Nanoparticle Oxidation in Three Dimensions by Chemically Sensitive Electron Tomography and *in Situ* Transmission Electron Microscopy

Weiwei Xia,[†,‡] Yang Yang,[§] Qingping Meng,[∥] Zhiping Deng,[⊥] Mingxing Gong,[†,⊥] Jie Wang,[⊥] Deli Wang,[⊥] Yimei Zhu,[∥] Litao Sun,[‡] Feng Xu,[*,‡] Ju Li,[*,§] and Huolin L. Xin[*,†]

[†]Center for Functional Nanomaterials and [∥]Condensed Matter Physics and Materials Science Department, Brookhaven National Laboratory, Upton, New York 11973, United States

[‡]SEU-FEI Nano-Pico Center, Key laboratory of MEMS of Ministry of Education, Southeast University, Nanjing 210096, China

[§]Department of Nuclear Science and Engineering and Department of Materials Science and Engineering, Massachusetts Institute of Technology, Cambridge, Massachusetts 02139, United States

[⊥]Key Laboratory of Material Chemistry for Energy Conversion and Storage, Ministry of Education, Hubei Key Laboratory of Material Chemistry and Service Failure, School of Chemistry and Chemical Engineering, Huazhong University of Science and Technology, Wuhan 430074, China

Supporting Information

ABSTRACT: **The formation of hollow-structured oxide nanoparticles is primarily governed by the Kirkendall effect. However, the degree of complexity of the oxidation process multiplies in the bimetallic system because of the incorporation of more than one element. Spatially dependent oxidation kinetics controls the final morphology of the hollow nanoparticles, and the process is highly dependent on the elemental composition. Currently, a theoretical framework that can predict how different metal elements result in different oxide morphologies remains elusive. In this work, utilizing a combination of state-of-the-art *in situ* environmental transmission electron microscopy and three-dimensional (3D) chemically sensitive electron tomography, we provide an *in situ* and 3D investigation of the oxidation mechanism of the Ni−Fe nanoparticles. The direct measurements allow us to correlate the 3D elemental segregation in the particles with the oxidation morphologies, that is, single-cavity or dual-cavity hollow structure, and multicavity porous structures. Our findings in conjunction with theoretical calculations show that metal concentration, diffusivity, and particle size are important parameters that dictate the mechanical and phase stabilities of the hollow oxide shell, which in turn determine its barrier properties and the final hollow oxide morphology. It sheds light on how to use multielemental oxidation to control morphology in nanomaterials and demonstrates the power of 3D chemical imaging.**

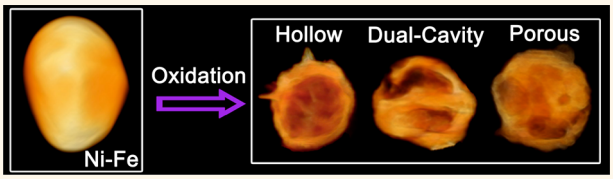

KEYWORDS: *3D electron tomography, internal oxidation, porosity, pinhole, Ni and Fe spinels*

Hollow nanomaterials[1−6] have attracted increasing interest[7] due to their potential applications in catalysis,[8−11] sensing,[12] energy storage,[13,14] and drug delivery.[4] Many works have focused on developing methods to control their morphology and composition, which in turn tune their properties.[8,15−18] Oxidation-induced hollow-nanostructured bimetallic oxides[17,19−21] is of particular importance, because the synthetic method is low-cost and scalable. Achieving a comprehensive understanding of the reaction mechanism and the transformation kinetics during the oxidation process is of great importance toward tailoring the morphology and properties of hollow or porous oxides. Unlike monometallic nanoparticles, where the oxidation process has been well-characterized by *in situ* X-ray and transmission electron microscopy methods, so far, a theory that can predict how multimetallic nanoparticles evolve during oxidation still remains elusive. Recent works have shed some light on the complexity, but the understanding is far from complete.[22] The difficulty of studying multimetallic oxidation lies in the evolution of three-dimensional (3D) heterogeneity in both

Received: March 22, 2018
Accepted: August 6, 2018
Published: August 6, 2018

DOI: 10.1021/acsnano.8b02170
ACS Nano 2018, 12, 7866−7874

structure and chemistry within the nanoparticles during oxidation.

In this work, utilizing a combination of state-of-the-art *in situ* environmental transmission electron microscope and 3D chemically sensitive electron tomography, we provide an *in situ* and 3D investigation of the size and composition-dependent oxidation of a Ni_xFe_{1-x} nanoparticle system, with varying x. With the tomography technique, we can unscramble the information that is lost in projected images and mappings. By tracking the oxidation process performed inside an environment transmission electron microscope (ETEM), we uncovered three types of reaction route that results in three different morphologies, that is, porous, dual-cavity, and hollow structures. The results demonstrate that the final morphology of the oxidized products is determined by the formation of pinholes in the oxide shell and voids at the core/shell interface. Statistical analysis shows that the resulting oxide morphology is strongly correlated with particle size and elemental composition: hollow products dominated the smaller particles, while the porous ones dominated the larger particles; meanwhile, the probability of forming porous structure decreases with increasing Fe concentration (in other words higher Ni concentration leads to more porous oxides). The stress and composition evolutions inside the particles appear to have strong impact on the stability of the oxide shell. Our theoretical modeling verifies this hypothesis and shows that these size and composition-dependent oxidation behaviors are very likely a result of the particle stress caused by heterogeneous phase distribution and concentration gradient. By combining all these techniques and theoretical analysis, we developed a framework that can predict the complex behavior in bimetallic and multimetallic systems, which can guide the rational synthesis of samples with different hollow morphologies.

RESULTS AND DISCUSSION

Electron Tomography of Fe–Ni Particles before and after Oxidation. Figure 1 shows 3D *ex situ* characterization of the Ni–Fe particles in the pristine (Figure 1a), fully oxidized (Figure 1b–d), and partially oxidized (Figure 1e) stages using electron tomography (see Methods Section). Figure 2 shows their corresponding 3D chemical structures reconstructed using chemically sensitive electron tomography (see Methods for details). The pristine particle features a round solid structure with relatively uniform Ni–Fe compositional distribution (Figures 1a and 2a, Video S1, and Figure S1), which demonstrates the bimetallic particles are structurally and chemically homogeneous before the oxidation reaction. After oxidation, however, we found that that round and solid metallic particles transform into a complex 3D structure (also see the chemical mappings in Figure S2). The structural complexity can be classified into three categories: (1) a single-cavity hollow structure, (2) a dual-cavity structure, and (3) a multicavity porous structure. The single-cavity hollow particles, in contrast to the dual-cavity and the porous particles, has a closed shell (see the cross sections in Video S2)—the shell wall is continuous with no cracks or pinholes. Because the self-diffusivity of oxygen is orders of magnitude slower than those of nickel and iron in their oxides (Figure S3a),[23−27] the solid oxide shell serves as an oxygen barrier to only allow the metals to diffuse outward, and therefore, it forms a hollow particle. On the one hand, this kinetics controlling oxidation behavior at the nanoscale has been well-explained by the Kirkendall effect.[7,28−31] On the other hand, the dual-cavity and porous

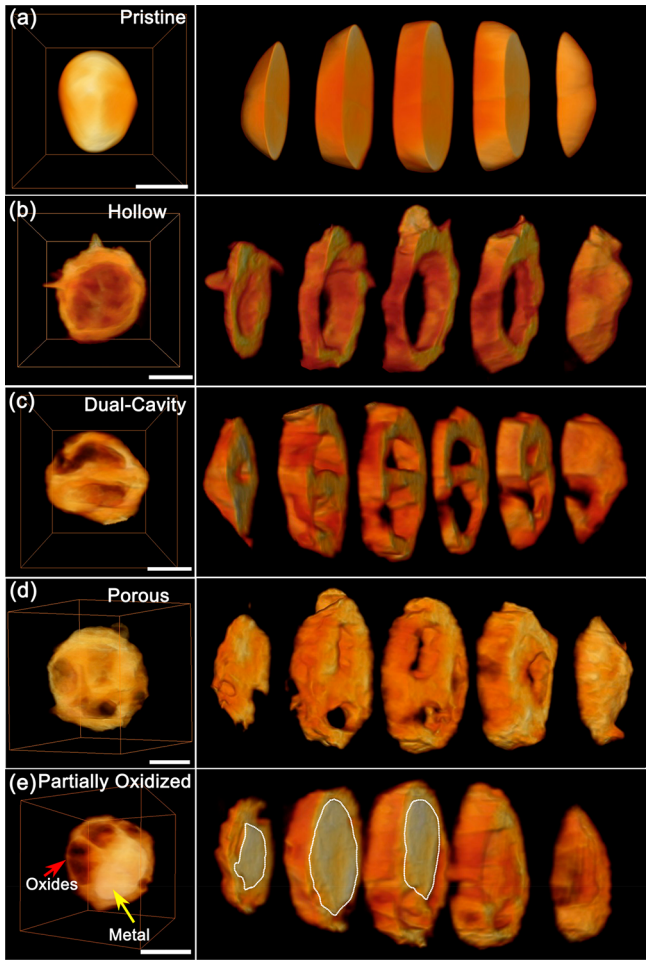

Figure 1. 3D ADF-STEM tomographic reconstruction of (a) pristine (see also Video S1), (b–d) fully oxidized (see also Videos S2, S3, and S4, respectively), and (e) partially oxidized (see also Video S5) particles. Fully oxidized products exhibit three different morphologies: (b) single-cavity hollow structure ; (c) dual-cavity structure; (d) multicavities porous structure. Scale bar, 50 nm.

particles feature multiple pinholes in the outer shell wall (Figure 1c,d and Videos S3 and S4). By reconstructing a partially oxidized particle (Figures 1e and 2b and Video S5), we obtain a frozen snapshot of these pinholes at the early development stage. It is worth noting that, on the lower-right of the particle, there is a pinhole that had just developed between the metal core/oxide shell interfaces. This pinhole would expose the metal core to the oxygen environment if the reaction continues.

In addition to the morphological complexity, the chemical structure of the oxidized particle also offers information regarding the structural formation mechanism. Figure 2c shows that the hollow particle has obvious chemical segregation with more iron segregating to the outer surface of the shell wall. This oxygen adsorption-induced segregation phenomenon is driven both by the diffusion kinetics and the oxidation thermodynamics (the Ellingham diagram of Fe, Ni oxides, which relate to the oxidation potential, is shown in Figure S3b)—iron diffuses faster than nickel and binds stronger with oxygen than nickel does. (The theory of oxygen adsorption-induced segregation is explained in detail in our previous study of the Ni–Co system.[22]) Therefore, iron segregation in this system can be used as a probe for where exposure to oxygen

DOI: 10.1021/acsnano.8b02170
ACS Nano 2018, 12, 7866–7874

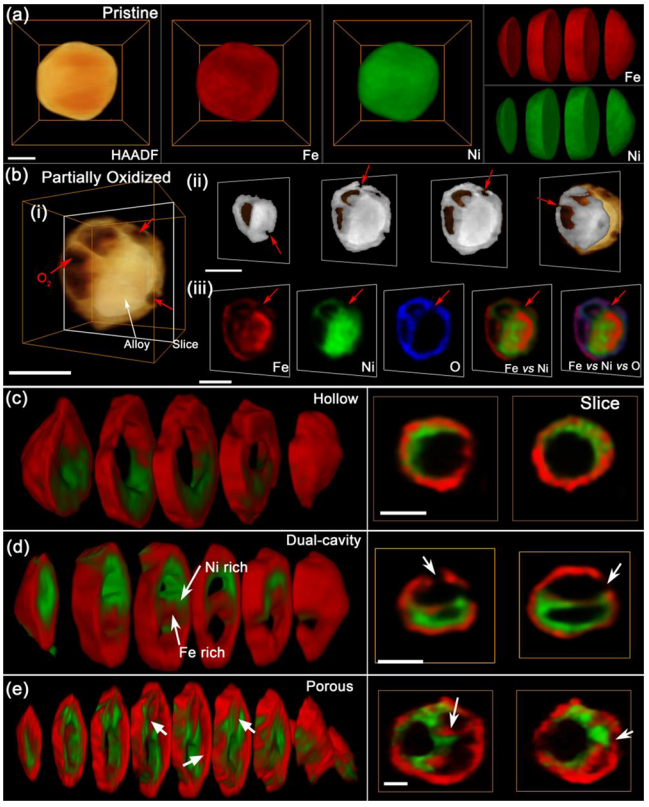

Figure 2. Chemically sensitive tomography of particles (a) before and (b) after partial and (c–e) full oxidation. Chemical segregation varies with the morphology of oxidized product, suggesting the spatial-dependent oxidation pathway differs in different morphology. Note the pinhole on the lower-right of the particle in (b). Scale bars are (a, b) 50 nm and (c–e) 20 nm.

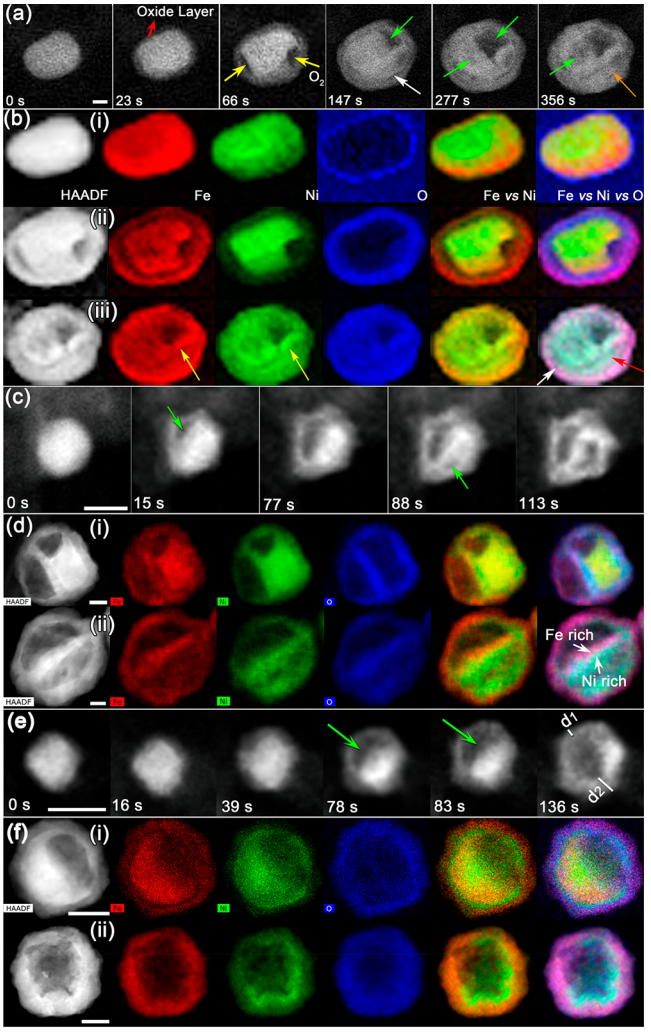

Figure 3. *In situ* observation of morphology and compositional changes during $Ni_{0.67}Fe_{0.33}$ oxidation. (a) Time-lapsed images showing the internal oxidation behavior during the porous structure formation process (see also Video S6). (b) The corresponding EELS mapping of Fe, Ni, and O at different oxidation stage. (c) Time-lapsed images show the formation process of the dual-cavity structure (see also Video S7). (d) EDS mappings in (d_i) partially and (d_{ii}) fully oxidized particles show the elemental segregation is different in the two cavities, which reflects the oxidation direction. (e) Time-lapsed images show the dynamic formation process of off-center hollow structure (see also Video S8). (f_i) The elemental distribution of a partially oxidized hollow structure. EDS mappings of a fully oxidized hollow structure shown in (f_{ii}), where Fe only concentrates on the outer shell, suggesting that this oxidation mechanism is dominated by the regular Kirkendall effect. Scale bar, 20 nm.

had happened. In the porous particles (Figure 2e), some of the interior surfaces as indicated by the arrow also show iron segregation. Particularly in the dual-cavity particle (Figure 2d), the cavity separator shows iron segregation to the side where the shell wall is discontinuous. These suggest that oxygen had infiltrated the broken cavity and induced iron segregation to the broken side.

All this evidence suggests that the pinhole formation in the shell wall during the oxidation process is key to the development of the complex internal oxidation microstructure. This aspect of the Ni–Fe system is similar to the Ni–Co system we previously reported: the development of pinholes allows infiltration of oxygen to the interior of the particles to allow internal oxidation.[22] However, we found the probability of occurrence of single-cavity hollow structure is high in the Ni–Fe system, as opposed to only ~5% in the Ni–Co case. The large difference between the two systems is surprising. To understand the mechanisms underlying the difference between the two systems, we next performed *in situ* investigation of the oxide formation process.

In Situ Environmental Study of the Formation of Different Oxide Morphologies. Figure 3a and Video S8 show the dynamic process of forming the multicavity porous structure during oxidation in oxygen at 650 °C inside the ETEM. After it was heated for 23 s in O_2, the pristine $Ni_{0.67}Fe_{0.33}$ particle was enclosed by a low-intensity layer marked by the red arrow, forming a core–shell structure. The low-intensity layer continued to grow thicker until reaching a critical shell thickness.[32] Subsequently, multiple voids simultaneously formed at the core/shell interface and separated the core from low-intensity shell, as the yellow arrows indicate. The positions where the voids nucleate and grow are influenced by the grain boundaries, as they play important roles of trapping vacancies and thus lead to a local development of voids.[7,33] Then, the metal core started to be oxidized inside the previously formed shell, and another shell appeared internally. The voids marked by the green arrows increased in size, and the shells grew thicker, whereas the previously formed voids marked by the yellow arrows

DOI: 10.1021/acsnano.8b02170
ACS Nano 2018, 12, 7866–7874

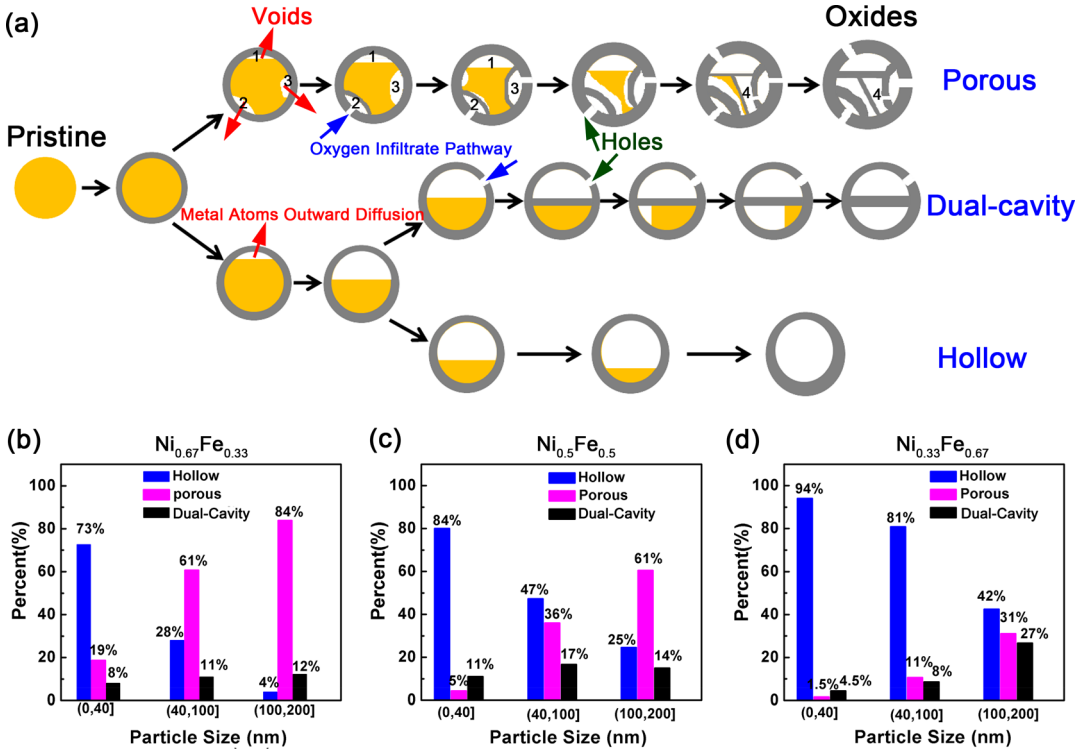

Figure 4. (a) Schematic cartoon compares the oxidation routes of forming different oxide morphologies. Two key factors that can determine the final morphology are (1) pinholes formation in the oxide shell wall and (2) voids formed at the core/shell interface. (b–d) Statistical analysis of how the oxide morphology is dependent on particle size and Ni/Fe composition: (b) $Ni_{0.67}Fe_{0.33}$, (c) $Ni_{0.5}Fe_{0.5}$, (d) $Ni_{0.33}Fe_{0.67}$.

decreased in size. As the oxidation process proceeded inside the second shell, the two shells continued to extend and eventually produced a porous structure with double shell walls. We can distinguish the oxidized volumes from the nonreacted metal by the *Z*-contrast intensities in high-angle annular dark-field scanning transmission electron microscopy (HAADF-STEM) images; higher intensity represents higher mass density, and the atomic mass density of Fe–Ni alloy is higher than their oxides.

To observe the elemental redistribution during the oxidation process *in situ*, we stopped heating the sample at a few representative stopping points and used electron energy loss spectroscopic (EELS) imaging in the scanning transmission electron microscopy (STEM) mode to acquire elemental maps. By comparing the maps of the particle before oxidation (Figure 3b_i) and at the partially oxidized stage in Figure 3b_{ii}, we can conclude that the low-intensity surface layer mentioned above is an oxide layer. Oxygen reacted with nickel and iron on the particle surface and formed a thin oxide layer first. Then iron and nickel diffused through the previously formed oxide layer and reacted with oxygen on the surface, resulting in an outer Fe-rich oxide shell. Afterward, the inner Ni-rich oxide layer formed as the oxidation process proceeds, as marked by the red arrow (Figure 3b_{iii}). From the EELS maps of the completely oxidized particle, we found the product featured obvious elemental segregation, where Fe concentrates on the outer surface of the shell and around the surface of internal cavities (indicated by the yellow arrows in Figure 3b_{iii}).

Figure 3c and Video S7 show the *in situ* formation process of a dual-cavity structure during $Ni_{0.67}Fe_{0.33}$ oxidation. Initially, the particle surface formed a thin oxide layer, which became thicker as the oxidation proceeds. Subsequently, a single void appeared at the interface of core/shell, which however stopped growing after several seconds. Later, another single void appeared at the position indicated by the green arrow and grew until the particle was completely oxidized. The growth behaves like the particle formed two hollow cavities that are separated by a separator. We can deduce that oxygen infiltrated inside the particle during the oxidation process as the separator is also oxide.

Figure 3d shows that, although the shell wall has higher iron composition in the outer surface and higher nickel composition in the inner surface, the elemental distribution is significantly different in the two cavities. The thickness and concentration of outer Fe-rich shell is much larger than inner Ni-rich shell in the first formed cavity, which is different from that in the second formed cavity. Similar elemental segregation in other dual-cavity particles was shown in Figure S4. In Figure S5, we used several particles with different degrees of oxidation to retrieve the information on elemental redistribution during the oxidation process. At the initial stage, Fe-rich oxide layer formed on the particle surface, and then Ni-rich oxide appeared in the inner wall as oxidation continues. After the first void stopped growing, an Fe-rich oxide separator formed. Subsequently, the second void appeared and started to grow, during which process the Ni-rich oxides formed at the separator and thickened in the shell. It eventually formed a dual-cavity particle with different elemental distributions. The oxidation direction can be easily distinguished, as the elemental segregation differs in the two cavities.

Time-lapsed *Z*-contrast STEM images displayed in Figure 3e show the *in situ* formation process of a hollow structure during $Ni_{0.67}Fe_{0.33}$ oxidation. A single void formed at the interface of core/shell, until the oxide layer reached a critical thickness.[32] The void grew bigger, and the shell became thicker, until the particle was oxidized completely, leaving an off-center cavity

DOI: 10.1021/acsnano.8b02170
ACS Nano 2018, 12, 7866–7874

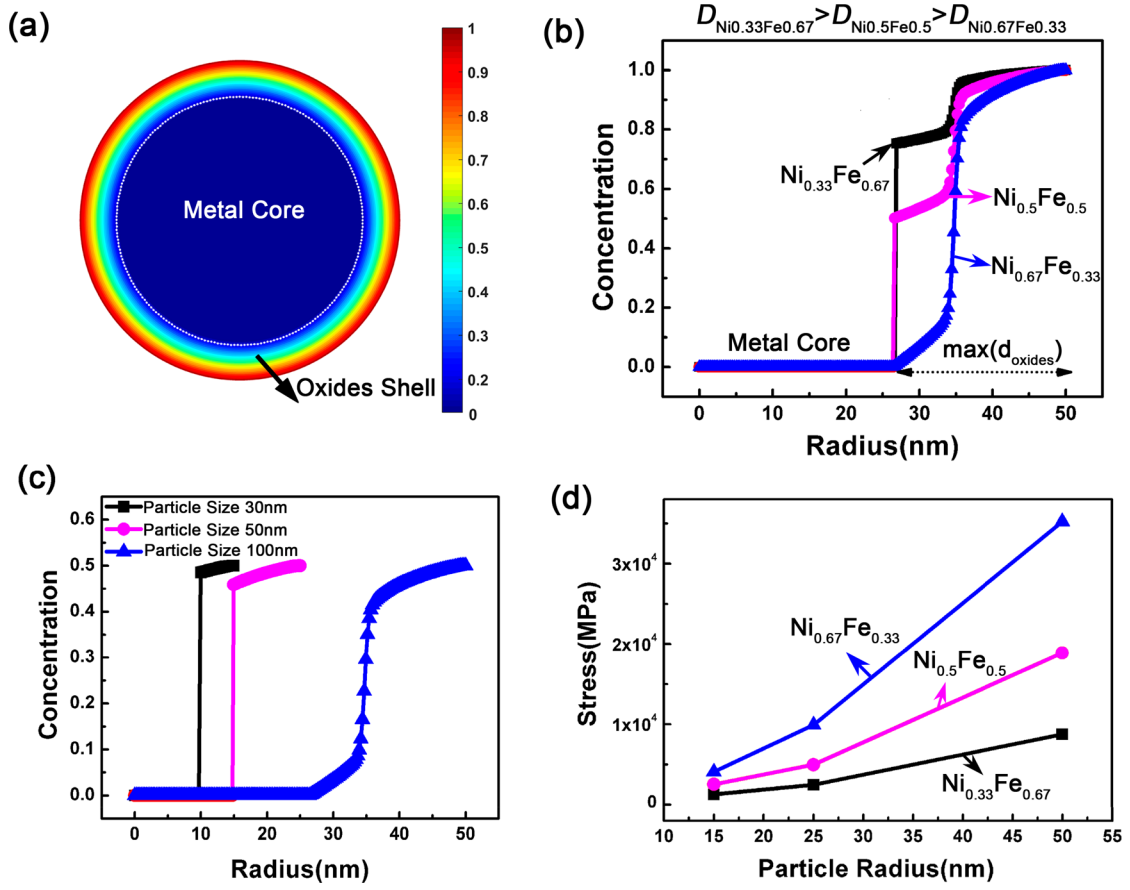

Figure 5. (a) Schematic illustration showing the nonuniform distribution of oxides concentration in the oxide shell of a spherical particle. (b) Distribution of oxides concentration in a 100 nm particle with different diffusion rates (in different alloy systems). (c) Distribution of oxides concentration in particles with different size (diffusion rate is kept the same). (d) Calculated surface stress in various-size particles with different diffusion rates.

inside the particle. Note that the oxidized shell wall adjacent to the point where the void nucleated changed negligibly, while the shell wall opposite to the void increased in thickness as the oxidation process proceeded, due to the more ample supply of out-diffusing metals on that side. We can clearly see that the oxidation behavior happens on the particle's external surface, which is different from the porous structure. The surface oxidation behaviors and formation of asymmetrical hollow structure can be repeatedly observed in different particles, as the images in Figure S6 and the dynamic oxidation processes in Video S8 show. STEM energy-dispersive X-ray spectroscopic (STEM-EDX) mappings displayed in Figure 4f indicate obvious elemental segregation—the hollow particle features a Fe-rich outer shell and a Ni-rich inner shell.

Summary of the Oxide Particle Formation Process. Figure 4a compares the formation process of different oxide morphologies. Initially, oxide layer forms and becomes thicker on the external surface of all particles. After the oxide layer reaches a critical thickness, oxidation mechanism starts to diverge. For porous particles, multiple voids simultaneously form at the interface between the oxide shell and metallic core. However, only the void (void 1) within the solid shell continues to grow, as metal atoms must diffuse outward through the solid oxide layer and react with oxygen. Meanwhile, other voids (void 2) stop growing and even become smaller, as a new oxide layer is produced and grows inside the particle, because the broken shell allows oxygen infiltration. As the oxidation process continues, the initially formed solid shell can fracture and further lead to more cavities (voids 3 and 4), in keeping with the behaviors reflected by the images in Figure 3a. It is reasonable to deduce that, even if multiple voids are generated, the particles would hollow out as a single-cavity structure if no pinhole/fracture forms in the exterior oxide shell wall.[33,34] That is to say, the formation of porous structure should be attributed to the combination of multiple voids formation at oxides/metal interface and fracture/pinhole formation in the exterior oxide shell wall, although the two could be causally related. In contrast, on the one hand, the dual-cavity structure is formed because only a single void was formed, and the exterior oxide shell wall broke on the single-void side. On the other hand, a single void enclosed by a solid shell results in hollow structure that has asymmetric shell thickness. The holes drawn in Figure 4a do exist in the 3D volume but cannot be observed in the projection images, as the shell inevitably overlaps with the core in two-dimensional (2D) projections. We draw the schematics here to summarize the formation process.

To exclude the electron-beam (e-beam) effect in the *in situ* oxidation experiments, we examined the sample under e-beam irradiation for 2 h, and we did not observe any perceivable change in both morphology and microstructure during the irradiation process (see Figure S7 in Supporting Information), which means our samples are relatively insensitive to e-beam

DOI: 10.1021/acsnano.8b02170
ACS Nano 2018, 12, 7866−7874

irradiation, although in many other cases the electron beam can induce local heating, knock-on damage, and coalescence.

Statistical Analysis of Composition and Size Dependency. Our experimental observation shows the occurrence of single-cavity hollow structure is high in the Ni−Fe system, as opposed to only ∼5% in the Ni−Co case we previously reported.[22] To understand the large difference between the two systems and provide a unified theory, we performed a systematical experiment and analyzed three different Ni/Fe compositions. To retrieve the statistical dependency of morphology on particle size, we imaged and analyzed more than 400 oxidized particles for each Fe/Ni composition—that is, $Ni_{0.67}Fe_{0.33}$, $Ni_{0.5}Fe_{0.5}$, and $Ni_{0.33}Fe_{0.67}$. These particles are alloys rather than intermetallic compounds, which have been verified by the powder X-ray diffraction (XRD) results in Figure S8a. The three compositional samples show the same host crystal structure (face-centered cubic (fcc) Fe−Ni, slight peak shift are caused by the varying contents of Fe, which dissolved into Ni) except weak body-centered cubic (bcc) Fe peaks are detected in the $Ni_{0.5}Fe_{0.5}$ and $Ni_{0.33}Fe_{0.67}$ systems, which, however, does not affect our statistically significant conclusions (see Figure S8 in Supporting Information for more details). We name the three alloy systems based on their nominal molar ratios of Fe and Ni, which are very close to the average atomic ratios measured by EDX mappings (see Figure S8b and the Method Section for more detail). As the results in Figure 4b−d show, the oxide particles' morphology is found to be size- and composition-dependent. The hollow structure dominates the smaller sizes, while the porous structure dominates the larger particles. The dual-cavity structure has relatively few occurrences and does not affect the size-dependent trend. Furthermore, the chance of forming porous structure decreases as the composition of Fe increases in Fe−Ni alloy, which is likely related to the change of diffusivity in different composition systems. As shown by our 3D and *in situ* images, the formation of different morphology particles is very likely determined by pinhole/crack formation in the exterior oxide shell. Thus, we can make a reasonable deduction that the formation of pinholes and voids are greatly affected by the particle sizes. Specifically, the probability of forming broken-shell walls and multiple voids for larger-sized particles/Ni-rich system is higher than that for smaller-sized/Fe-rich system particles due to Weibull statistics.

The voids formation behavior depends on the balance of the formation rate and migration rate of vacancies.[35] If vacancy formation determined by the outward diffusion of the metallic atoms through the oxide layer is significantly slower than the vacancy migration rate determined by the self-diffusion of metallic atoms in the alloy core, single void appears. Otherwise, multiple voids form.[35] The diffusion coefficients for different particles in the same alloy system and reaction conditions are identical, and therefore the generation of voids should mainly be ascribed to the difference in diffusion distance. For larger particles, before metallic atoms diffuse a long distance to condense all the vacancies into one single void, the outward diffusion of atoms through oxide layer has already increased the local vacancy concentration in different locations and thus is more likely to produce multiple voids.[32]

Theoretical Modeling of Stress Cracking in the Exterior Oxide Shell. The nucleation and growth of crack/pinholes in the oxide shell wall is likely induced by the stress[36] that was built up during the oxidation process. Here, we used a simple kinetic model that includes both size and composition dependencies to estimate the particle stress by calculating the oxides concentration (oxidation) gradient. We model that there is an oxide concentration gradient from the outer surface to the inner surface of the oxide shell (Figure 5a). The gradient is dependent on the self-diffusivity of the transition metals through their oxides (see Methods Section for mathematical details). The oxide gradient is less if the diffusion rate is higher (Figure 5b). Here the effective diffusivity is a combined effect of Ni and Fe. As the self-diffusivity of Fe in its oxide compounds is order of magnitude higher than that of Ni, the diffusion rate D for $Ni_{0.67}Fe_{0.33}$, $Ni_{0.5}Fe_{0.5}$, and $Ni_{0.33}Fe_{0.67}$ ranks as follows: $D_{Ni0.33Fe0.67} > D_{Ni0.5Fe0.5} > D_{Ni0.67Fe0.33}$. As the diffusion rate of oxygen is much slower than metallic atoms in the oxide layer, we assume only the outward diffusion of the transition metals contribute to the effect. As shown in Figure 5b, there is a much larger concentration gradient for $Ni_{0.67}Fe_{0.33}$, because it has the lowest diffusion rate.

The particle size also plays an important role in our model. As shown in Figure 5c, the longer diffusion distance results in larger oxides concentration difference under the same diffusion rate. The stress at surface as a function of particle size and diffusion rate (in different composition system) is shown in Figure 5d. We can find that surface stress increases with increasing particle size, and this result gives a good explanation to why bigger particle favors forming pinholes in the shell wall (and then porous structure). At the same time, we also find the system with a faster diffusion rate has lower surface stress. The result is in agreement with our experimental observation that the occurrence of porous particles decrease with the increase of Fe concentration, as the diffusivity of Fe is much higher than Ni through the oxide (as Figure S3 shows). This surface stress model captures the major contributions to the size- and composition-dependent oxidation behaviors in Fe−Ni alloy system. Finally, this model reconciles the fact that the Ni−Co system has less occurrence of single-cavity hollow structure—Ni diffuses slower than Co in the oxide layer and results in larger stress in the shell.[32,12,13,37,38]

Apart from oxidation kinetics, the thermodynamics of the final oxidized products may also play an important role in causing cracking and the resulting porosity (Figures S9 and S10 in Supporting Information). For the Fe-rich system, the alloy core, which was enclosed with an Fe oxide layer, can transform into an Fe-rich inverse spinel structure (e.g., $NiFe_2O_4$), which is stable during high-temperature oxidation. However, after Fe is depleted completely, it is energetically unfavorable for a Ni-rich oxide to maintain an inverse spinel crystal structure, because $Ni_xFe_{3-x}O_4$ ($x > 1$) is not stable.[39] Instead, Ni-rich inverse spinel structure will lose oxygen and tend to phase separate into Fe-rich oxides and NiO precipitate,[39] which is evidenced by our XRD result showing that the content of NiO is increased in the $Ni_{0.67}Fe_{0.33}$ system (Figure S10). Phase separation developed with thickening oxide can lead to strain mismatch along the phase boundary and cracking. Therefore, it is very likely that the phase instability of the nickel-rich oxide is a cocontributing factor to the formation of pinholes in an oxide shell wall, leading to repeated internal oxidation. It also agrees with our observation that the Ni-rich system has a higher chance of forming a porous structure, while Fe-rich system is prone to producing hollow structures with solid shells.

DOI: 10.1021/acsnano.8b02170
ACS Nano 2018, 12, 7866−7874

CONCLUSION

In summary, we systematically investigated the oxidation behavior of Ni−Fe alloy nanoparticles with the assistance of *in situ* ETEM imaging, 3D mass contrast, and chemically sensitive tomography. We revealed that the complexity of oxide structural evolution is controlled by phase, composition, and stress evolutions. Our stress-cracking model of the oxide shell wall provides a unified theory that reconciles our experiments findings for different bimetallic systems. The results provided guiding principles for synthesizing hollow-structured oxides that could potentially widen their applications in different fields.

METHODS

Preparation of Ni−Fe/CNT. The carbon nanotube-supported Ni−Fe-based alloy particles were obtained via a simple impregnation−reduction method. Typical for $Ni_{0.5}Fe_{0.5}$ alloy, 108 mg of $NiCl_2{\cdot}6H_2O$, 90.3 mg of $FeCl_2{\cdot}4H_2O$ (molar ratio = 1:1), and 87 mg of carbon nanotubes (CNTs) were dispersed in a 25 mL beaker by using purified water (10 mL) as solvent. The mixture underwent magnetic stirring and ultrasonic dispersion at 60 °C, until the solvent was evaporated. To ensure complete drying, the mixture was put into a vacuum drying oven at 40 °C overnight. After it was fully milled in an agate mortar, the powder was calcined in a tube furnace at 350 °C for 3 h under H_2 atmosphere to obtain an alloy structure, which was labeled as $Ni_{0.5}Fe_{0.5}$/CNT. The $Ni_{0.67}Fe_{0.33}$/CNT and $Ni_{0.33}Fe_{0.67}$/CNT samples were obtained via the same method and varying molar ratio of $NiCl_2{\cdot}6H_2O$ and $FeCl_2{\cdot}4H_2O$ to 2:1 and 1:2.

Ex Situ Oxidation of Ni−Fe/CNT in Air. The as-prepared Ni_xFe/CNT powders were placed at ceramic crucibles and then transferred into tube furnace. After it was oxidized at different elevated temperatures (350, 400, and 450 °C) for 4 h with a ramp rate of 1 °C/min for heating, we removed the samples from the furnace and left them to cool to room temperature. Then the oxidized powers were ultrasonically dispersed into methanol and dropped onto Cu grid coated with lacy carbon for further TEM characterization.

In Situ oxidation of Ni−Fe/CNT in ETEM. We used a field-emission ETEM (FEI Titan 80−300 keV, operated at 300 keV) equipped with an objective lens spherical aberration corrector to perform the *in situ* oxidation experiments. The as-prepared Ni_xFe/CNT powders were first ultrasonically dispersed into methanol and then drop-casted onto a nonporous silicon nitride TEM membrane that would be transferred into a DENS solutions Micro Electromechanical System (MEMS) device-based heating holder subsequently. The local heating on the MEMS device is based on the Joule heating of a micropatterned metal heater. The resistance of the heater has a linear response to temperature in the range from room temperature to 1300 °C. The manufacturer had already measured the relationship between the temperature and the resistance of the heater prior to experiments (The temperature was measured using Raman scattering of the silicon substrate). Before the *in situ* oxidation experiments were performed, we also calibrated the temperature by inputting the initial resistance and manufacture parameter of the MEMS chip, respectively. The temperature that can be calculated by measuring the heater resistance was recorded by the software Digiheater. Before it was heated, we preflow oxygen for 20 min, and the pressure in the objective area is set to 0.2 Torr. When performing *in situ* oxidation experiments, the temperature was elevated to 650 °C from 23 °C in 5 min. The *in situ* annular dark-field scanning transmission electron microscopy (ADF-STEM) images were acquired in the STEM mode, and the electron energy loss spectroscopy (EELS) data were acquired by a Gatan Tridiem spectrometer.

ADF-STEM and EDX Chemical Tomographic Reconstruction. A 200 keV field-emission S/TEM (FEI Talos F200X) equipped with a four-quadrant EDX detector was used to perform the chemically sensitive electron tomography. ADF-STEM tilt series images were recorded from −74° to 74° with 2° intervals, while the chemically sensitive tilt series data were acquired from −75° to 75° with 5° or 7° intervals. No noticeable mass loss or radiation damage was observed during the data acquisition process. The 3D tomograms were reconstructed using a Matlab script package (e-Tomo) written by Robert Hovdenand visualized by Avizo.

Theory Calculating Methods. We used Cahn−Hilliard equation[40]

$$\frac{\partial c}{\partial t} = \nabla M c \nabla(\Delta\mu) \tag{1}$$

to describe the evolution of the oxides concentration (c) inside a particle. M is the mobility tensor, which relates to the diffusion of Fe and Ni ions (here, they were taken to be isotropic and constant). The chemical potential $\Delta\mu$

$$\Delta\mu = \frac{\partial f}{\partial c} - \kappa\nabla^2 c \tag{2}$$

derives from the homogeneous concentration-dependent free energy f and the Cahn−Hilliard gradient energy coefficient κ. The free energy includes the chemical free energy that is dependent on the chemical composition and the elastic energy arising from the lattice misfit strain between oxides and metallic cores. In our simulation, the maximum oxides concentration was rescaled to 1. With the definition of chemical potential from chemical free energy, $\frac{\partial f}{\partial c} = k_B T \ln a$, where $a = \gamma c$ and $\gamma = 1$ (dilute limit), eq 1 can be simplified into general diffusion equation if other effects are ignored.[41] For the isotropic approximation, the elastic energy is

$$f_{el}(c) = \left(\frac{K}{2} - \frac{\mu}{3}\right)(\varepsilon_{rr} + 2\varepsilon_{\theta\theta} - 3\varepsilon^0(c))^2 + \mu(\varepsilon_{rr} - \varepsilon^0(c))^2 + 2\mu(\varepsilon_{\theta\theta} - \varepsilon^0(c))^2 \tag{3}$$

where $\varepsilon^0_{ij}(c) = \Delta\varepsilon^0_{ij}c$; $\Delta\varepsilon^0_{ij}$ is the maximum misfit strain between oxides and metallic cores; K and μ are elastic constants;[42] ε_{rr} and $\varepsilon_{\theta\theta}$ are radial strain and axial strain, respectively. In our program code, we changed loop number after each step of oxidation to calculate the effect of diffusion rate.

ASSOCIATED CONTENT

Supporting Information

The Supporting Information is available free of charge on the ACS Publications website at DOI: 10.1021/acsnano.8b02170.

HAADF and TEM images, illustrated distribution of iron and nickel, plotted data indicating temperature-dependent diffusion coefficients, Ellingham diagrams, EDX and EELS mappings, XRD patterns (PDF)

Video of the slices of a reconstructed pristine particle (AVI)

Video of the slices of a reconstructed hollow fully oxidized particle (AVI)

Video of the slices of a reconstructed dual-cavity fully oxidized particle (AVI)

Video of the slices of a reconstructed porous fully oxidized particle (AVI)

Video of the slices of a reconstructed partially oxidized particle (AVI)

Video of the dynamic oxidation process of porous particles (AVI)

Video of the dynamic oxidation process of dual-cavity particles (AVI)

Video of dynamic oxidation process of hollow particles (AVI)

DOI: 10.1021/acsnano.8b02170
ACS Nano 2018, 12, 7866−7874

AUTHOR INFORMATION

Corresponding Authors

*E-mail: fxu@seu.edu.cn. (F.X.)
*E-mail: liju@mit.edu. (J.L.)
*E-mail: hxin@bnl.gov. (H.L.X.)

ORCID

Yang Yang: 0000-0002-0025-5914
Deli Wang: 0000-0003-2023-6478
Litao Sun: 0000-0002-2750-5004
Ju Li: 0000-0002-7841-8058
Huolin L. Xin: 0000-0002-6521-868X

Author Contributions

H.L.X. conceived the idea. W.X. performed the *in situ* oxidation experiments, EELS/EDX acquisition and analysis, as well as 3D tomography reconstruction. The alloy particles were synthesized by J.W. and D.W., while Q.M. and Y.Z. performed theoretical modeling.

Notes

The authors declare no competing financial interest.

ACKNOWLEDGMENTS

This research is supported by the Center for Functional Nanomaterials, which is a U.S. Department of Energy (DOE) Office of Science Facility, at Brookhaven National Laboratory, under Contract No. DE-SC0012704. W.X. and F.X. are also supported by the Fundamental Research Funds for the Central Universities, and the Research Innovation Program for College Graduates of Jiangsu Province (KYLX16_0218), the "Scientific Research Foundation of Graduate School of Southeast University" (YBJJ1660), the National Basic Research Program of China (2015CB352106), the National Natural Science Foundation of China (11774051, 61574034), a scholarship from the China Scholarship Council (CSC) (201606090069, 201406250041). M.G. is supported by the CSC (201706160151). Q.M. and Y.Z. are supported by DOE-BES, Materials Sciences and Engineering Division, under Contract No. DESC0012704. J.L. acknowledges support by NSF ECCS-1610806.

REFERENCES

(1) Ma, Y.; Huo, K.; Wu, Q.; Lu, Y.; Hu, Y.; Hu, Z.; Chen, Y. Self-Templated Synthesis of Polycrystalline Hollow Aluminium Nitride Nanospheres. *J. Mater. Chem.* **2006**, *16*, 2834−2838.

(2) Bernard Ng, C. H.; Tan, H.; Fan, W. Y. Formation of Ag_2Se Nanotubes and Dendrite-like Structures from UV Irradiation of a CSe_2/Ag Colloidal Solution. *Langmuir* **2006**, *22*, 9712−9717.

(3) Tan, H.; Li, S.; Fan, W. Y. Core-Shell and Hollow Nanocrystal Formation *via* Small Molecule Surface Photodissociation; Ag@Ag_2Se as an Example. *J. Phys. Chem. B* **2006**, *110*, 15812−15816.

(4) Gao, J.; Liang, G.; Zhang, B.; Kuang, Y.; Zhang, X.; Xu, B. FePt@CoS_2 Yolk-Shell Nanocrystals as a Potent Agent to Kill HeLa Cells. *J. Am. Chem. Soc.* **2007**, *129*, 1428−1433.

(5) Zhou, S.; Varughese, B.; Eichhorn, B.; Jackson, G.; McIlwrath, K. Pt-Cu Core-Shell and Alloy Nanoparticles for Heterogeneous NO*x* Reduction: Anomalous Stability and Reactivity of a Core-Shell Nanostructure. *Angew. Chem.* **2005**, *117*, 4615−4619.

(6) Lou, X. W.; Deng, D.; Lee, J. Y.; Feng, J.; Archer, L. A. Self-Supported Formation of Needlelike Co_3O_4 Nanotubes and Their Application as Lithium-Ion Battery Electrodes. *Adv. Mater.* **2008**, *20*, 258−262.

(7) Yin, Y.; Rioux, R. M.; Erdonmez, C. K.; Hughes, S.; Somorjai, G. A.; Alivisatos, A. P. Formation of Hollow Nanocrystals Through the Nanoscale Kirkendall Effect. *Science* **2004**, *304*, 711−714.

(8) Song, H. M.; Anjum, D. H.; Sougrat, R.; Hedhili, M. N.; Khashab, N. M. Hollow Au@Pd and Au@Pt Core−Shell Nanoparticles as Electrocatalysts for Ethanol Oxidation Reactions. *J. Mater. Chem.* **2012**, *22*, 25003−25010.

(9) Kim, S. W.; Kim, M.; Lee, W. Y.; Hyeon, T. Fabrication of Hollow Palladium Spheres and Their Successful Application to the Recyclable Heterogeneous Catalyst for Suzuki Coupling Reactions. *J. Am. Chem. Soc.* **2002**, *124*, 7642−7643.

(10) Bai, Z.; Xu, P.; Chao, S.; Yan, H.; Cui, Q.; Niu, L.; Yang, L.; Qiao, J. A Facile One-Step Preparation of a Pd−Co Bimetallic Hollow Nanosphere Electrocatalyst for Ethanol Oxidation. *Catal. Sci. Technol.* **2013**, *3*, 2843−2848.

(11) Guo, S.; Dong, S.; Wang, E. Three-Dimensional Pt-on-Pd Bimetallic Nanodendrites Supported on Graphene Nanosheet: Facile Synthesis and Used as an Advanced Nanoelectrocatalyst for Methanol Oxidation. *ACS Nano* **2010**, *4*, 547−555.

(12) Zhao, X.; Cao, M.; Hu, C. Thermal Oxidation Synthesis Hollow MoO_3 Microspheres and Their Applications in Lithium Storage and Gas-Sensing. *Mater. Res. Bull.* **2013**, *48*, 2289−2295.

(13) Lavela, P.; Tirado, J. L. $CoFe_2O_4$ and $NiFe_2O_4$ Synthesized by Sol−Gel Procedures for Their Use as Anode Materials for Li Ion Batteries. *J. Power Sources* **2007**, *172*, 379−387.

(14) Sun, S.; Li, S.; Wang, S.; Li, Y.; Han, L.; Kong, H.; Wang, P. Fabrication of Hollow $NiCo_2O_4$ Nanoparticle/Graphene Composite for Supercapacitor Electrode. *Mater. Lett.* **2016**, *182*, 23−26.

(15) Zhou, J.; Liu, J.; Wang, X.; Song, J.; Tummala, R.; Xu, N. S.; Wang, Z. L. Vertically Aligned Zn_2SiO_4 Nanotube/ZnO Nanowire Heterojunction Arrays. *Small* **2007**, *3*, 622−626.

(16) Jin fan, H.; Knez, M.; Scholz, R.; Nielsch, K.; Pippel, E.; Hesse, D.; Zacharias, M.; Gösele, E. Monocrystalline Spinel Nanotube Fabrication Based on the Kirkendall Effect. *Nat. Mater.* **2006**, *5*, 627−631.

(17) Jaffari, G. H.; Ceylan, A.; Ni, C.; Shah, S. I. Enhancement of Surface Spin Disorder in Hollow $NiFe_2O_4$ Nanoparticles. *J. Appl. Phys.* **2010**, *107*, 013910.

(18) Liu, J.; Xue, D. Thermal Oxidation Strategy towards Porous Metal Oxide Hollow Architectures. *Adv. Mater.* **2008**, *20*, 2622−2627.

(19) Wang, C. M.; Schreiber, D. K.; Olszta, M. J.; Baer, D. R.; Bruemmer, S. M. Direct *in Situ* TEM Observation of Modification of Oxidation by the Injected Vacancies for Ni-4Al Alloy Using a Microfabricated Nanopost. *ACS Appl. Mater. Interfaces* **2015**, *7*, 17272−17277.

(20) Gao, X.; Wang, J.; Zhang, D.; Nie, K.; Ma, Y.; Zhong, J.; Sun, X. Hollow $NiFe_2O_4$ Nanospheres on Carbon Nanorods as a Highly Efficient Anode Material for Lithium Ion Batteries. *J. Mater. Chem. A* **2017**, *5*, 5007−5012.

(21) Wang, Y.; Su, D.; Ung, A.; Ahn, J. H.; Wang, G. Hollow $CoFe_2O_4$ Nanospheres as a High Capacity Anode Material for Lithium Ion Batteries. *Nanotechnology* **2012**, *23*, 055402.

(22) Han, L.; Meng, Q.; Wang, D.; Zhu, Y.; Wang, j.; Du, X.; Stach, E. A.; Xin, H. L. Interrogation of Bimetallic Particle Oxidation in Three Dimensions at the Nanoscale. *Nat. Commun.* **2016**, *7*, 13335.

(23) Volpe, M. L.; Reddy, J. Cation Self-Diffusion and Semiconductivity in NiO. *J. Chem. Phys.* **1970**, *53*, 1117−1125.

(24) Dubois, C.; Monty, C.; Philibert, J. Oxygen Self-Diffusion in NiO Single Crystals. *Philos. Mag. A* **1982**, *46*, 419−433.

(25) Himmel, L.; Mehl, R. F.; Birchenall, C. E. Self-Diffusion of Iron in Iron Oxides and the Wagner Theory of Oxidation. *JOM* **1953**, *5*, 827−843.

(26) Castle, J. E.; Surman, P. L. Self-Diffusion of Oxygen in Magnetite. Techniques for Sampling and Isotopic Analysis of Micro Quantities of Water. *J. Phys. Chem.* **1967**, *71*, 4255−4259.

(27) Crouch, A. G.; Robertson, J. Creep and Oxygen Diffusion in Magnetite. *Acta Metall. Mater.* **1990**, *38*, 2567−2572.

(28) Ha, D. H.; Moreau, L. M.; Honrao, S.; Hennig, R. G.; Robinson, R. D. The Oxidation of Cobalt Nanoparticles into Kirkendall-Hollowed CoO and Co_3O_4: The Diffusion Mechanisms and Atomic Structural Transformations. *J. Phys. Chem. C* **2013**, *117*, 14303−14312.

DOI: 10.1021/acsnano.8b02170
ACS Nano 2018, 12, 7866−7874

(29) Nakamura, R.; Tokozakura, D.; Nakajima, H.; Lee, J. G.; Mori, H. Hollow Oxide Formation by Oxidation of Al and Cu Nanoparticles. *J. Appl. Phys.* **2007**, *101*, 074303.
(30) Peng, S.; Sun, S. Synthesis and Characterization of Monodisperse Hollow Fe_3O_4 Nanoparticles. *Angew. Chem., Int. Ed.* **2007**, *46*, 4155−4158.
(31) Nakamura, R.; Matsubayashi, G.; Tsuchiya, H.; Fujimoto, S.; Nakajima, H. Formation of Oxide Nanotubes *via* Oxidation of Fe, Cu and Ni Nanowires and Their Structural Stability: Difference in Formation and Shrinkage Behavior of Interior Pores. *Acta Mater.* **2009**, *57*, 5046−5052.
(32) Railsback, J. G.; Johnston-Peck, A. C.; Wang, J.; Tracy, J. B. Size-Dependent Nanoscale Kirkendall Effect During the Oxidation of Nickel Nanoparticles. *ACS Nano* **2010**, *4*, 1913−1920.
(33) El Mel, A. A.; Buffiere, M.; Tessier, P. Y.; Konstantinidis, S.; Xu, W.; Du, K.; Wathuthanthri, I.; Choi, C. H.; Bittencourt, C.; Snyders, R. Highly Ordered Hollow Oxide Nanostructures: The Kirkendall Effect at the Nanoscale. *Small* **2013**, *9*, 2838−2843.
(34) Yang, Y.; Yang, R. B.; Fan, H. J.; Scholz, R.; Huang, Z.; Berger, A.; Qin, Y.; Knez, M.; Gosele, U. Diffusion-Facilitated Fabrication of Gold-Decorated Zn_2SiO_4 Nanotubes by a One-Step Solid-State Reaction. *Angew. Chem., Int. Ed.* **2010**, *49*, 1442−1446.
(35) Nakamura, R.; Lee, J. G.; Mori, H.; Nakajima, H. Oxidation Behaviour of Ni Nanoparticles and Formation Process of Hollow NiO. *Philos. Mag.* **2008**, *88*, 257−264.
(36) Evans, H. E. Cracking and Spalling of Protective Oxide Layers. *Mater. Sci. Eng., A* **1989**, *120*, 139−146.
(37) Yang, S.; Yang, J.; Chung, Y.; Kwon, Y. Pd-Bi Bimetallic Catalysts Including Polyvinylpyrrolidone Surfactant Inducing Excellent Formic Acid Oxidation Reaction and Direct Formic Acid Fuel Cell Performance. *Int. J. Hydrogen Energy* **2017**, *42*, 17211−17220.
(38) Liu, Q.; Lai, L.; Fu, X.; Zhu, F.; Sun, J.; Rong, H.; He, M.; Chen, Q.; Xu, Z. Solvothermal Synthesis of $CoFe_2O_4$ Hollow Spheres. *J. Mater. Sci.* **2007**, *42*, 10113−10117.
(39) Shafer, M. W. Preparation and Properties of Ferrospinels Containing Ni^{3+}. *J. Appl. Phys.* **1962**, *33*, 1210−1211.
(40) Cahn, J. W.; Hilliard, J. E. Free Energy of a Nonuniform System. *J. Chem. Phys.* **1958**, *28*, 258−267.
(41) Ferguson, T. R.; Bazant, M. Z. Nonequilibrium Thermodynamics of Porous Electrodes. *J. Electrochem. Soc.* **2012**, *159*, A1967−A1985.
(42) Reichmann, H. J.; Jacobsen, S. D. High-Pressure Elasticity of a Natural Magnetite Crystal. *Am. Mineral.* **2004**, *89*, 1061−1066.

DOI: 10.1021/acsnano.8b02170
ACS Nano 2018, 12, 7866−7874

Bimetallic Nanoparticle Oxidation in Three Dimensions by Chemically Sensitive Electron Tomography and *In-Situ* Transmission Electron Microscopy

Weiwei Xia[1,2], Yang Yang[3], Qingping Meng[4], Zhiping Deng[5], Mingxing Gong[1,5], Jie Wang[5], Deli Wang[5], Yimei Zhu[4], Litao Sun[2], Feng Xu[2]*, Ju Li[3]*, Huolin L. Xin[1]*

1. Center for Functional Nanomaterials, Brookhaven National Laboratory, Upton, New York 11973, United States.

2. SEU-FEI Nano-Pico Center, Key laboratory of MEMS of Ministry of Education, Southeast University, Nanjing 210096, China.

3. Department of Nuclear Science and Engineering and Department of Materials Science and Engineering, Massachusetts Institute of Technology, Cambridge, Massachusetts 02139, United States.

4. Condensed Matter Physics and Materials Science Department, Brookhaven National Laboratory, Upton, New York 11973, United States.

5. Key Laboratory of Material Chemistry for Energy Conversion and Storage (Huazhong University of Science and Technology), Ministry of Education, Hubei Key Laboratory of Material Chemistry and Service Failure, School of Chemistry and Chemical Engineering, Huazhong University of Science and Technology, Wuhan 430074, China.

*Correspondence should be addressed to fxu@seu.edu.cn, liju@mit.edu, or hxin@bnl.gov

Video S1. A series of cross-sections of a reconstructed pristine particle.

Video S2. A series of cross-sections of a reconstructed hollow fully oxidized particle.

Video S3. A series of cross-sections of a reconstructed dual-cavity fully oxidized particle.

Video S4. A series of cross-sections of a reconstructed porous fully oxidized particle.

Video S5. A series of cross-sections of a reconstructed partially oxidized particle.

Video S6. Dynamic process of porous particles formation during oxidation.

Video S7. Dynamic process of two-cavity particles formation during oxidation.

Video S8. Dynamic process of hollow particles formation during oxidation.

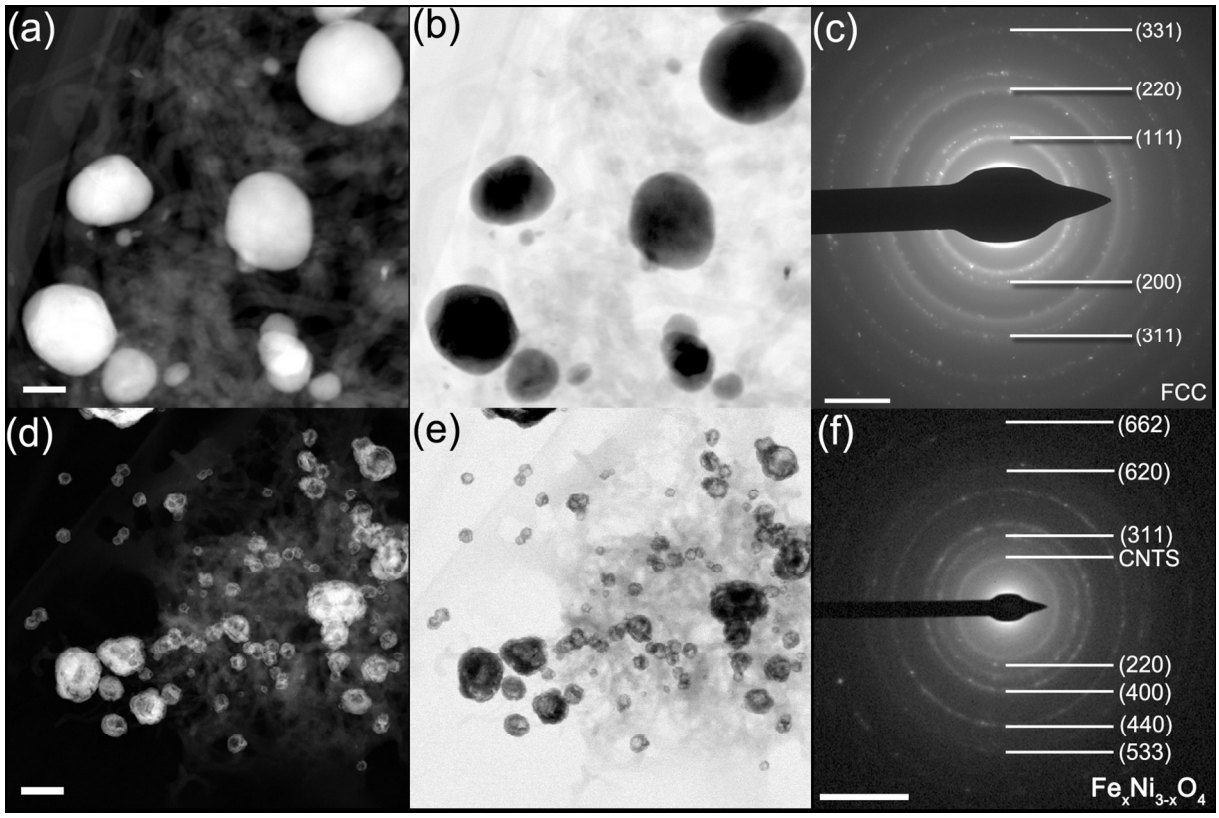

Figure S1. HAADF image of particles before (a) and after (d) oxidation. TEM image of particles before (b) and after (e) oxidation. Diffraction pattern of particles before (c) and after (f) oxidation. Scale bar, (a,b) 50nm, (d,e) 200nm, (c,f) 5 1/nm.

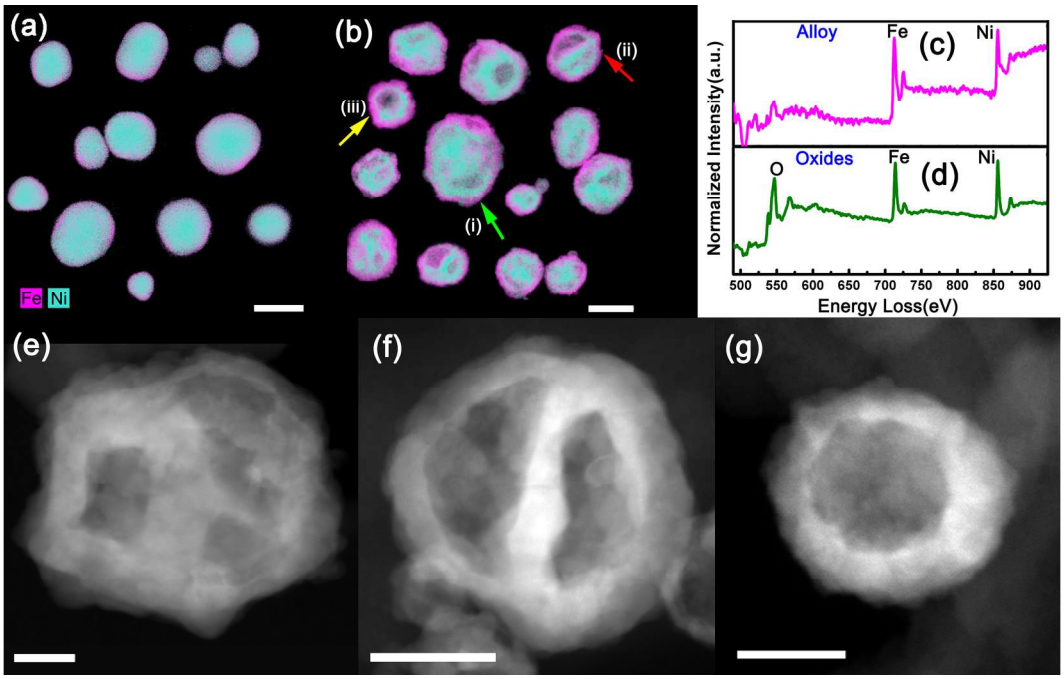

Figure S2. Chemical mapping of iron and nickel distribution in different $Ni_{0.67}Fe_{0.33}$ nanoparticles (a) before and (b) after complete oxidation. Different color arrows in (b) represent different morphologies—(i) porous (e), (ii) dual-cavity (f), (iii) hollow (g). Electron energy loss spectrum (EELS) extracted from the spectral image of nanoparticle (c) before and (d) after oxidation. Scale bar, (a,b) 100nm; (e-g) 20nm.

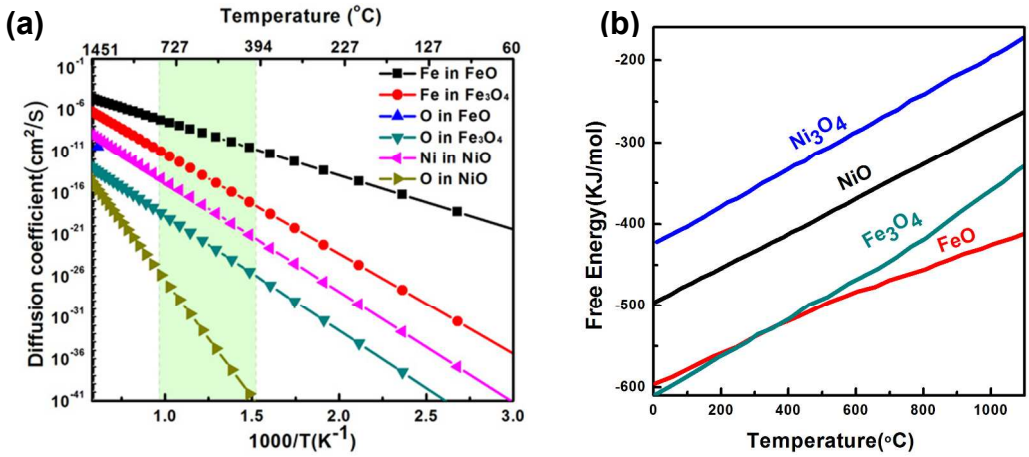

Figure S3. (a) Temperature-dependent diffusion coefficient of O and metal Fe, Ni in their oxides. The green area corresponds to the temperature in our experiments. (b) Ellingham diagrams of iron and nickel oxides at one atmosphere pressure. According to this, the outward segregation phenomenon of iron oxides is also likely determined by the larger driving force for Fe oxidation, as a result of the difference in oxidation potential between Fe and Ni.

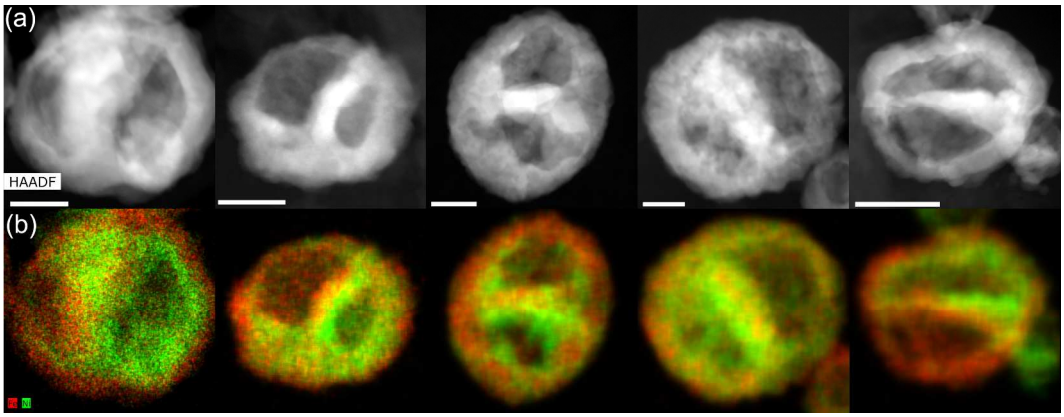

Figure S4. (a) HAADF images and (b) corresponding EDX Fe-Ni color-mix mappings of fully oxidized two-cavity particles, showing obvious elements segregation in two cavities.

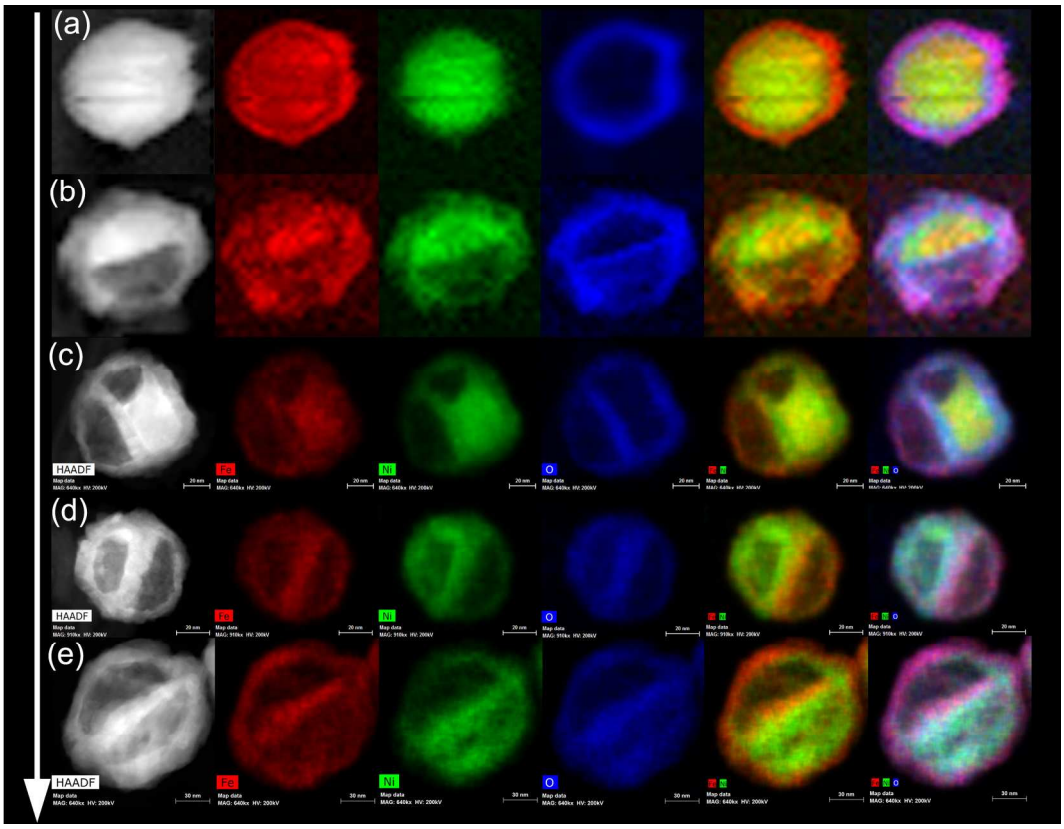

Figure S5. EDX mappings of particles at different oxidation degree during dual-cavity structure formation process.

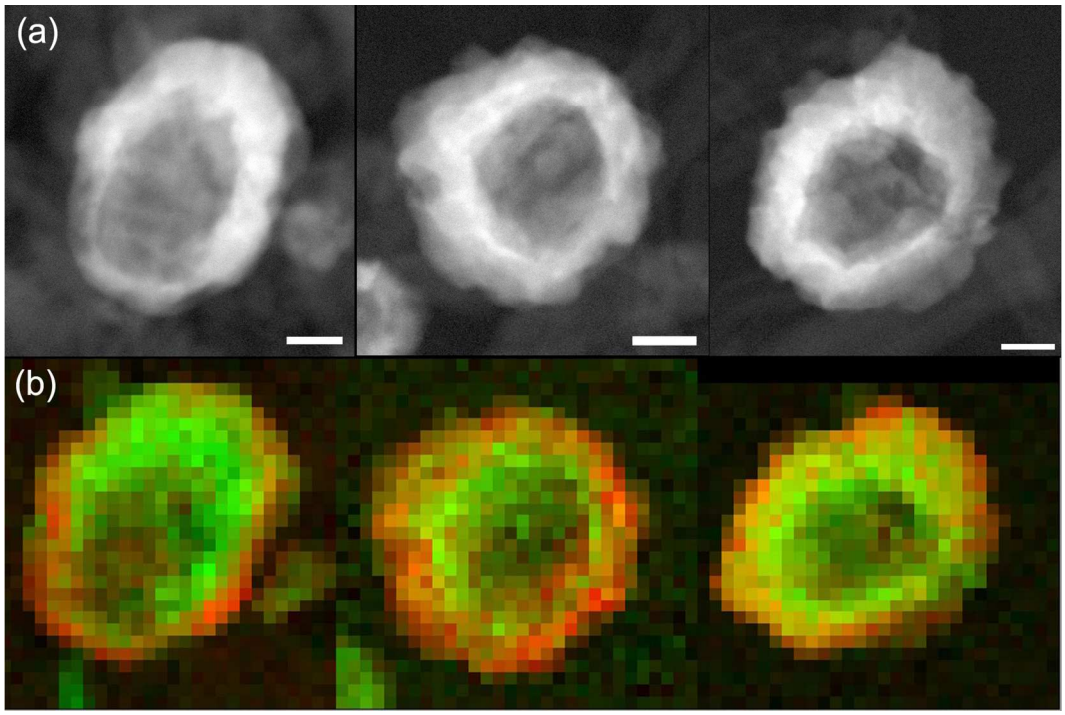

Figure S6. (a) HAADF images and (b) corresponding EELS Fe-Ni color-mix mappings of fully oxidized hollow particles, showing obvious elements segregation along oxidation direction. Scale bar, 20nm.

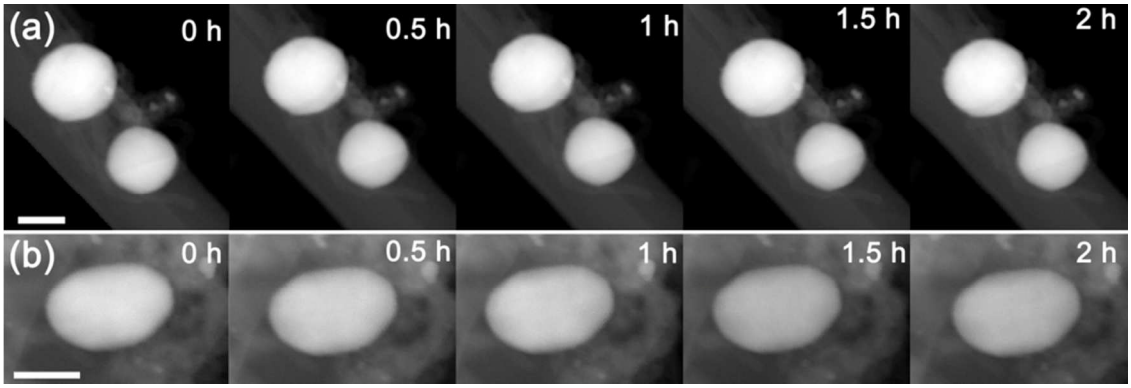

Figure S7. HAADF images show the particles at different irradiation time, from that we found the samples are robust and insensitive to electron beam. Scale bar, 50nm.

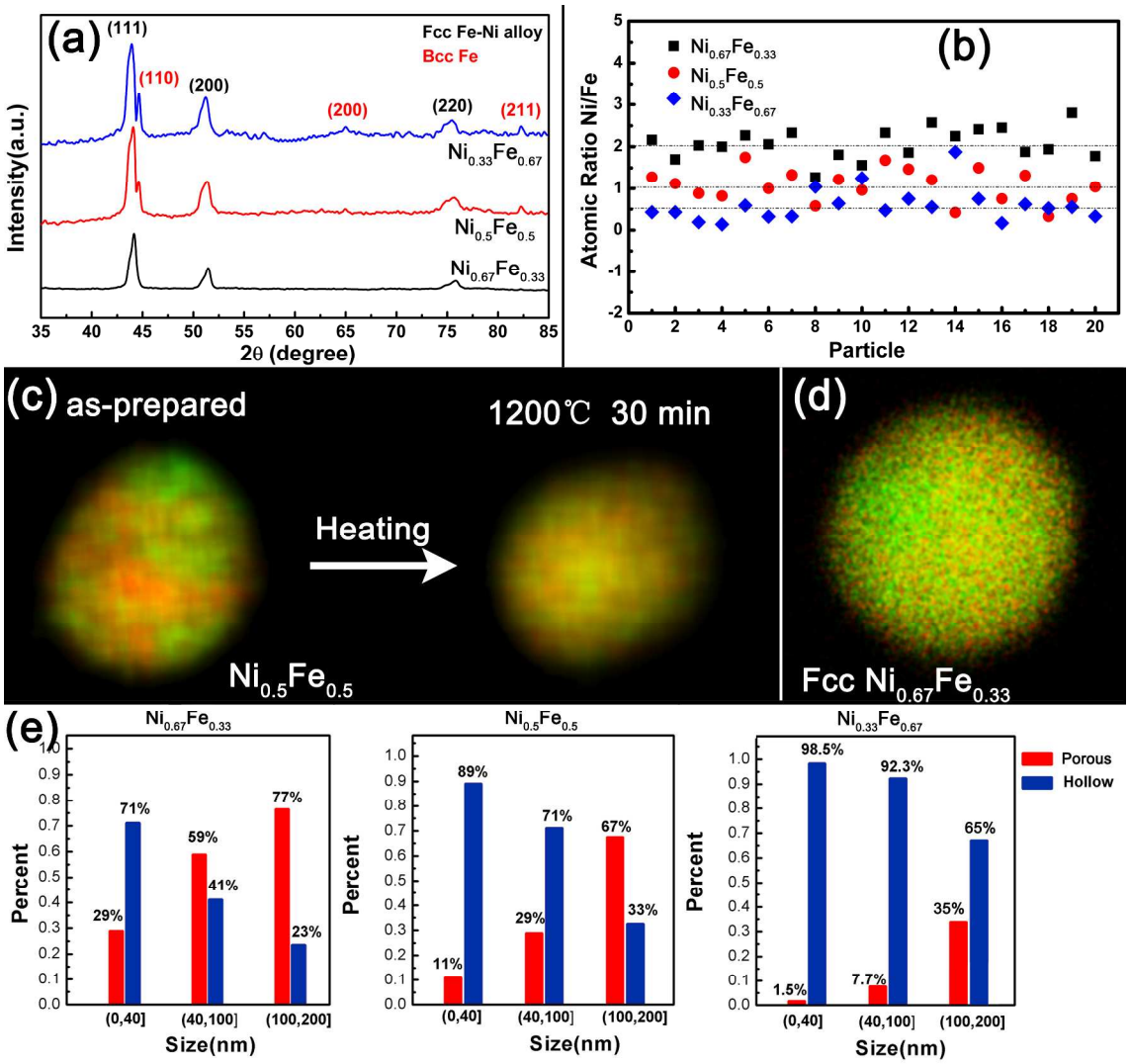

Figure S8. (a) X-ray diffraction (XRD) patterns and (b) compositional atomic ratios (Ni:Fe) in different particles of the as-prepared pristine samples. The calculated average atomic ratio is 2.07±0.08,1.02±0.07 and 0.59±0.07 for $Ni_{0.67}Fe_{0.33}$, $Ni_{0.5}Fe_{0.5}$ and $Ni_{0.33}Fe_{0.67}$ system (very close to the nominal ratios), respectively.(c) Phase transformation of a typical $Ni_{0.5}Fe_{0.5}$ particle under 1200°C for 30 minutes. (d) The fcc $Ni_{0.67}Fe_{0.33}$ particle is shown here for comparison. (e) Statistics of oxides morphology of the heated particles in different size and system after the *in-situ* oxidation of the heated samples.

From the powder XRD pattern in Figure S8a we find the three samples show same host crystal structure (fcc Fe-Ni, slight peak shift were caused by the varying contents of Fe which was dissolved into Ni) except little difference that weak bcc Fe peaks were detected in the $Ni_{0.5}Fe_{0.5}$ and $Ni_{0.33}Fe_{0.67}$ systems. This phase separation is inevitable during sample synthesis processes, which is in accordance with the Fe-Ni binary phase diagram and our previous work.

Although the crystal structures in three samples are not exactly same, we do not think the appearance of bcc iron peaks is a main factor that affects our conclusion that the morphology is size/composition-depended. The reasons are as followings. (1). $Ni_{0.5}Fe_{0.5}$ and $Ni_{0.33}Fe_{0.67}$ show the same crystal structure but they also exhibit obvious difference in the occurrence of porous structures, as the same way as $Ni_{0.67}Fe_{0.33}$ and $Ni_{0.5}Fe_{0.5}$ system do. (2) To further exclude the effects of little difference in crystal structure, we heated the samples at 1200°C for more than 30 minutes before performed the *in-situ* experiments, in which the Fe atoms can further dissolve into Ni and form pure fcc structure (in keeping with the Ni-Fe phase diagram). Atypical particle (Fe:Ni=1:1) that has been transferred from separate phase to pure fcc structure under elevated temperature is shown in Figure S8c-8d. (The fcc $Ni_{0.67}Fe_{0.33}$ particle is shown here for comparison)

The samples were cooled down to room temperature for about 30 minutes after the phase transformation was done, then we started to perform the *in-situ* experiments under the same experimental conditions as mentioned in the manuscript. After oxidizing the samples, we did the statistics of morphology of oxidized particles under different size ranges and systems (the dual-cavity structures show very little occurrence and we counted it as hollow structures here), as shown in Figure S8e. From the statistics results that displayed in the following figures, we found it exhibits the similar trends as the oxides after ex-situ oxidation of the as-prepared samples show (The occurrence of porous structure is high in Ni-rich system, while the occurrence of hollow structure is high in Fe-rich system). These results further confirmed that the effect of little difference in crystal structure can be negligible in our works. The two main parameters that affect the oxidation pathways and oxides morphologies are size and composition in particles.

The measured average ratio Ni:Fe is 2.07±0.08,1.02±0.07 and 0.59±0.07 for $Ni_{0.67}Fe_{0.33}$, $Ni_{0.5}Fe_{0.5}$ and $Ni_{0.33}Fe_{0.67}$ system (close to the nominal ratios), respectively. These results verify that there are composition differences for different system. Although the composition for each particle in one system is not exactly the same, it does not affect the size/composition-depended oxidation behavior because we get the results from large number of statistical data-more than 400 particles for each system.

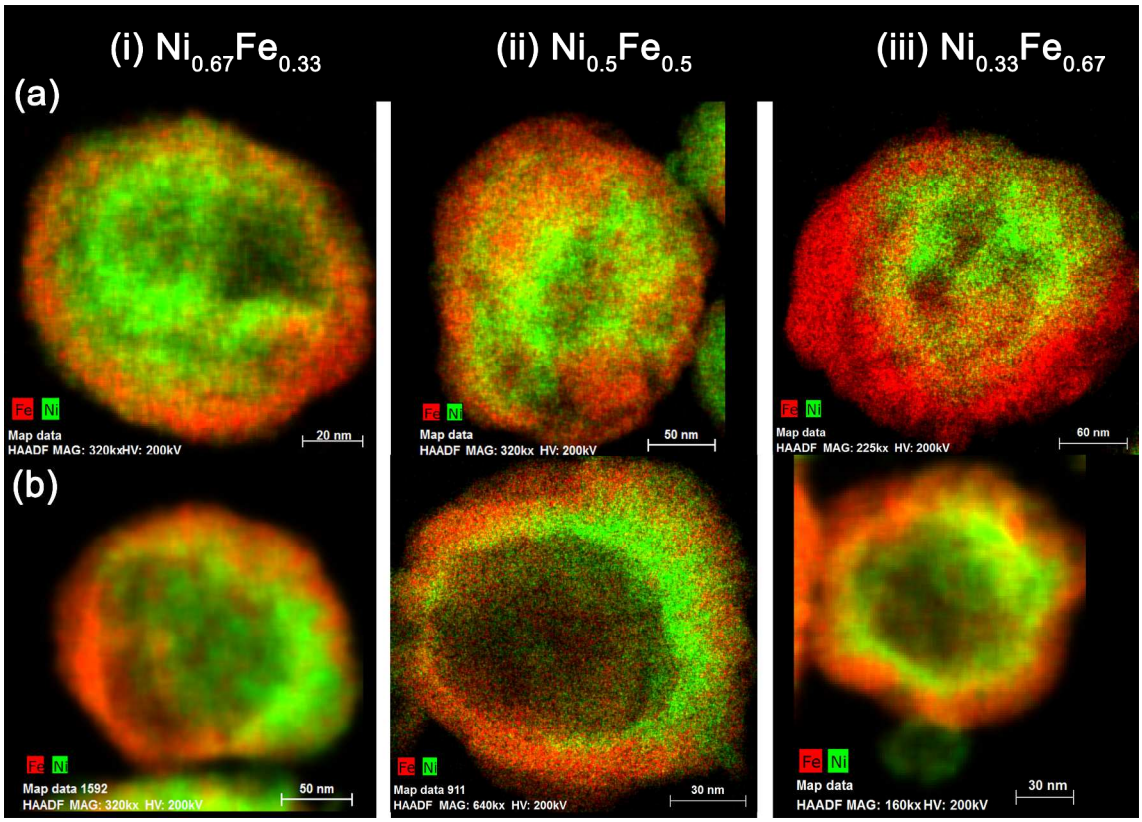

Figure S9. EDS elemental Fe, Ni mappings of oxidized particles in different composition system (i) $Ni_{0.67}Fe_{0.33}$; (ii) $Ni_{0.5}Fe_{0.5}$; (iii) $Ni_{0.33}Fe_{0.67}$. (a, b) represents porous and hollow structure, respectively. From that we can find the elements distribution is independent of the alloy composition.

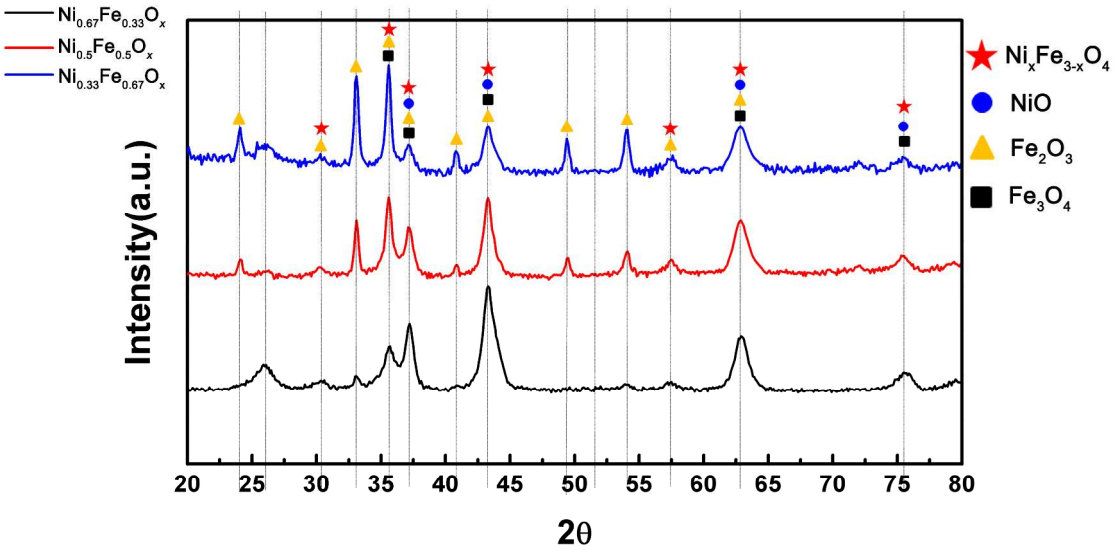

Figure S10. XRD results of the oxidized products in the three composition systems.